

# **Determination of the beam asymmetry $\Sigma$ in $\eta$ - and $\eta'$ -photoproduction using Bayesian statistics**

JAKOB MICHAEL KRAUSE

Masterarbeit in Physik

angefertigt im Helmholtz-Institut für Strahlen- und  
Kernphysik

vorgelegt der

Mathematisch-Naturwissenschaftlichen Fakultät  
der  
Rheinischen Friedrich-Wilhelms-Universität  
Bonn

Sep 2022

DRAFT

I hereby declare that this thesis was formulated by myself and that no sources or tools other than those cited were used.

Bonn, .....  
Date .....  
Signature

1. Gutachterin: JUN. PROF. DR. ANNIKA THIEL
2. Gutachter: PROF. DR. JOCHEN DINGFELDER

DRAFT

# Contents

---

<b>1</b>	<b>Introduction</b>	<b>1</b>
1.1	Photoproduction of Pseudoscalar Mesons . . . . .	4
1.2	Measurement of Polarization Observables . . . . .	5
1.3	Introduction to BAYESIAN statistics . . . . .	5
1.3.1	Frequentist Approach . . . . .	5
1.3.2	Bayesian approach . . . . .	5
1.3.3	Combining inferences . . . . .	5
1.4	Motivation and Structure of this Thesis . . . . .	5
<b>2</b>	<b>Experimental Setup</b>	<b>7</b>
2.1	Production of polarized high energy photon beam . . . . .	8
2.1.1	Goniometer . . . . .	9
2.1.2	Tagging system . . . . .	9
2.2	Liquid hydrogen target . . . . .	10
2.3	Detector system . . . . .	11
2.3.1	Inner detector . . . . .	11
2.3.2	Crystal Barrel and forward detector . . . . .	12
2.3.3	MiniTAPS . . . . .	13
2.3.4	ČERENKOV detector . . . . .	14
2.3.5	Flux monitoring . . . . .	14
2.4	Trigger . . . . .	15
2.5	Software and Monte Carlo . . . . .	15
2.6	Datasets . . . . .	15
<b>3</b>	<b>Event selection</b>	<b>17</b>
3.1	Reconstruction of events . . . . .	18
3.2	Preselection and charge cut . . . . .	18
3.3	Time of particles . . . . .	19
3.4	Kinematic constraints . . . . .	21
3.4.1	Derivation of cut conditions . . . . .	21
3.4.2	Determination of cut ranges . . . . .	22
3.4.3	Quality of event selection . . . . .	27
3.5	Investigation of background and additional cuts . . . . .	29
3.5.1	Inspecting plausibility of background reactions . . . . .	29
3.5.2	Misidentification of background reactions . . . . .	32
3.5.3	Examination of additional cuts . . . . .	37

3.6	Summary of event selection . . . . .	40
3.6.1	Reaction $\gamma p \rightarrow p\eta' \rightarrow p\gamma\gamma$ . . . . .	40
3.6.2	Reaction $\gamma p \rightarrow p\eta \rightarrow p\gamma\gamma$ . . . . .	41
<b>4</b>	<b>Extraction of the beam asymmetries <math>\Sigma_\eta</math> and <math>\Sigma_{\eta'}</math></b>	<b>43</b>
4.1	Methods . . . . .	44
4.1.1	Event yield asymmetries . . . . .	44
4.1.2	Event based fit . . . . .	47
4.2	Determination of $\Sigma_\eta$ using Bayesian statistics . . . . .	50
4.2.1	Application of methods to toy Monte Carlo data . . . . .	50
4.2.2	Application of methods to data . . . . .	59
4.2.3	Discussion . . . . .	62
4.3	Determination of $\Sigma_{\eta'}$ . . . . .	64
4.3.1	Application of event based fit to toy Monte Carlo data . . . . .	64
4.3.2	Application of event based fit to data . . . . .	70
4.3.3	Systematic error . . . . .	74
<b>5</b>	<b>Discussion</b>	<b>79</b>
5.1	Comparison of results to existing data . . . . .	79
5.2	Comparison of results to PWA calculations . . . . .	81
5.3	Final discussion of methods . . . . .	83
<b>6</b>	<b>Summary and outlook</b>	<b>85</b>
<b>A</b>	<b>Additional plots and calculations</b>	<b>87</b>
A.1	Statistical error for the asymmetry $A(\phi)$ . . . . .	87
A.2	Kinematic variables for each bin . . . . .	89
A.2.1	Coplanarity . . . . .	89
A.2.2	Polar angle difference . . . . .	91
A.2.3	Missing mass . . . . .	93
A.2.4	Invariant mass . . . . .	95
<b>B</b>	<b>Discussion of binned fits</b>	<b>97</b>
<b>C</b>	<b>Investigation of posteriors without truncation</b>	<b>99</b>
<b>Bibliography</b>		<b>103</b>
<b>List of Figures</b>		<b>109</b>
<b>List of Tables</b>		<b>115</b>



## CHAPTER 2

# Experimental Setup

In this work the beam asymmetry  $\Sigma$  is determined in the reactions  $\gamma p \rightarrow p\eta$  and  $\gamma p \rightarrow p\eta'$ , requiring a polarized photon beam and an unpolarized proton target. It is convenient to study photoproduction off a fixed target and investigate the resonances that occur in the process. The analyzed data was taken at the CBELSA/TAPS experiment located in Bonn at the EElectron Stretcher Accelerator (ELSA). In this chapter the different parts of the CBELSA/TAPS experiment that are used for the measurement of the beam asymmetry  $\Sigma$  will be presented. Figure 2.1 shows an overview of the experimental hall. All mentioned parts are discussed in detail in the following High energy electrons extracted from ELSA

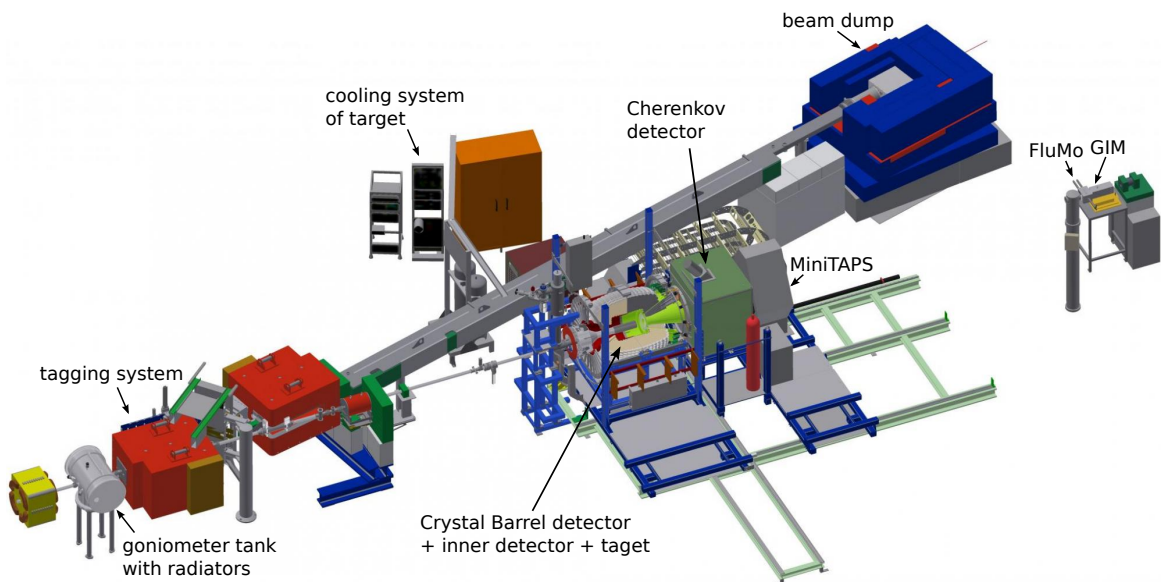


**Figure 2.1:** Overview of the experimental hall of the CBELSA/TAPS experiment. The electron beam from ELSA enters at the top right. M. GRÜNER in [Afz19]

are used to produce a polarized photon beam using the *bremssstrahlung* process (see 2.1.1). After they have been energy tagged (see 2.1.2) these photons then interact with the fixed target material (see Section 2.2) so that hadronic resonances may be excited that will decay via the strong interaction

under the emission of mesons. The resulting decay products can then be measured with a system of electromagnetic calorimeters and scintillators that is especially suited for the detection of photons (see Section 2.3). The analogue measurements are only saved for offline analysis if detector signals meet certain trigger conditions which is only the case for reactions that are of interest (see Section 2.4). This way the amount of unwanted background is minimized already during the process of data taking. Once data acquisition is finished the data may be investigated with the help of analysis software and Monte Carlo simulations tailored to the needs of the CBELSA/TAPS experiment (see Section 2.5).

## 2.1 Production of polarized high energy photon beam

To measure polarization observables in photoproduction reactions a polarized photon beam is needed which can be created using *coherent bremsstrahlung*. Bremsstrahlung is the dominating interaction of high energy ( $\mathcal{O}(1 \text{ GeV})$ ) electrons with matter [Leo94]. Electrons are decelerated in the COLOUMB field of heavy nuclei and radiate real photons, see Figure 2.2.

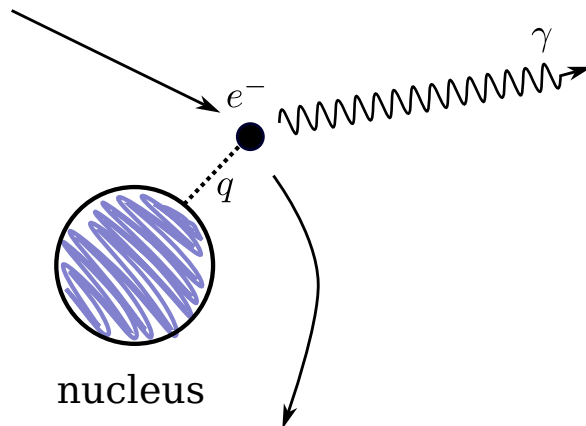


**Figure 2.2:** Illustration of the bremsstrahlung process: An electron  $e^-$  is deflected in the COLOUMB field of a nucleus in the radiator material. A photon  $\gamma$  is emitted and so the momentum  $q$  is transferred.

To conserve momentum there has to be a momentum transfer  $q$  which is negligibly small compared to the nucleon mass. If an amorphous radiator is used incoherent bremsstrahlung is produced with a continuous spectral distribution proportional to  $1/E_\gamma$ , according to the BETHE-HEITHLER cross section [Hei54]. Since the structure of nuclei in the amorphous radiator does not exhibit any periodicity, the electric field vector will not prefer any particular direction, resulting in a net polarization degree of zero for the photon beam. To achieve non-vanishing polarization degrees a crystal with periodic placement of nuclei may be used as radiator. Then, coherent bremsstrahlung is produced; the crystal can absorb the recoil only for discrete momenta  $q_n$  meeting the LAUE condition [Dem10] of the crystal lattice. This enables constructive interference between different bremsstrahl photons and at the same time fixes the deflection plane of incoming electrons, resulting in a coherent polarized photon beam. Incoherent bremsstrahlung may still occur due to impurities in the crystal structure, so that the total bremsstrahlung cross section off a crystal radiator  $\sigma_{\text{crystal}}$  is the sum of a coherent ( $\sigma_{\text{coherent}}$ ) and an incoherent ( $\sigma_{\text{incoherent}}$ ) part

$$\sigma_{\text{crystal}} = \sigma_{\text{coherent}} + \sigma_{\text{incoherent}}. \quad (2.1)$$

The process of bremsstrahlung can be modeled using ANalytical Bremsstrahlung (ANB) calculations [Nat+03]. ANB intensity spectra for a crystal and amorphous radiator are shown in Figure 2.3 on the left hand side. The right hand side shows the enhancement spectrum, which is given by dividing the two spectra. One observes that the bremsstrahlung intensity spectrum obtained from a crystal radiator

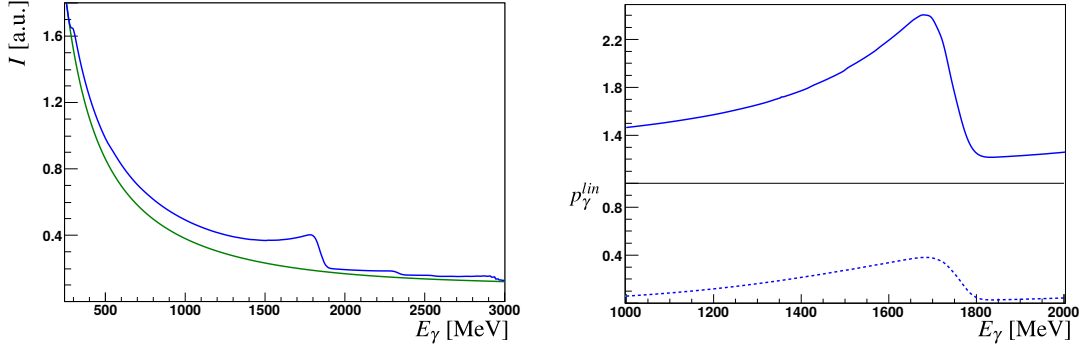


**Figure 2.3:** Left: Incoherent (green) and crystal (blue) bremsstrahlung intensities as a function of the photon energy. Right: The enhancement spectrum is given as the ratio of crystal to incoherent intensity spectrum. The dashed line at the bottom shows the calculated polarization degree. Both spectra are generated using ANB calculations. Taken from [Afz19].

is in general enhanced relative to the incoherent spectrum obtained from an amorphous radiator. In fact, using ANB calculations, the polarization degree can be determined from the enhancement spectrum. The characteristic drop in intensity in the intensity spectrum obtained from the crystal radiator is referred to as the coherent edge. It occurs because the photon energy in the kinematically allowed region of the recoil momentum that will lead to coherent bremsstrahlung is limited. The relative alignment of the radiation crystal to the electron beam determines the position of the coherent edge.

### 2.1.1 Goniometer

In order to determine the beam polarization from enhancement spectra, a diamond radiator as well as an amorphous radiator are required. Several radiators as well as beam diagnostics tools mounted inside a rotating aluminum wheel are part of the goniometer [Els+09], resting inside a vacuum tank. Depending on whether linearly polarized or unpolarized photons are needed either copper radiators of different thickness or a diamond radiator, which is located in the center of the wheel, are inserted into the beam axis, see Figure 2.4. In case a circularly polarized photon beam is required, a MØLLER polarimeter [Kam10] is used, which is also shown in Figure 2.4. The goniometer can be rotated in all directions allowing precise alignment with the incoming electron beam from ELSA.

### 2.1.2 Tagging system

Once the impinging electrons from ELSA have scattered off the radiator their energy is determined in order to measure the energy of the created photons. This is possible because the initial electron energy  $E_0 = 3.2 \text{ GeV}$  is known from ELSA. Thus, the photon Energy  $E_\gamma$  is given by subtracting the

energy of the recoil electrons  $E_e$  from  $E_0$ <sup>1</sup>

$$E_\gamma = E_0 - E_e. \quad (2.2)$$

The recoiling electrons are deflected towards the tagging system [For10] consisting of 96 overlapping scintillator bars and 480 scintillating fibers using the magnetic field of a dipole magnet with a field strength of 1.5 T. The bending radius of the electrons depends on their momenta is uniquely defined by the tagger hit position. With the position of the deflected electrons and the magnetic field strength,  $E_e$  can thus be determined. For an initial energy  $E_0 = 3.2$  GeV the scintillator bars cover an energy range of  $560\text{ MeV} < E_\gamma < 3100\text{ MeV}$  with an energy resolution of  $0.1\%E_\gamma$ - $6\%E_\gamma$ . The fibers additionally improve the energy resolution in the energy range  $416\text{ MeV} < E_\gamma < 2670\text{ MeV}$  to  $0.1\%E_\gamma$ - $0.4\%E_\gamma$ . Photomultipliers are used for the readout of the tagger bars and fibers, realizing a time resolution of  $^2\text{FWHM}_{\text{bar}} = 635\text{ ps}$  and  $\text{FWHM}_{\text{fiber}} = 1.964\text{ ns}$  [Har08]. Any electrons that have not interacted with the radiator material are deflected by another dipole magnet towards the beam dump, see Figure 2.1. Figure 2.5 shows a top-down view of the tagging system.

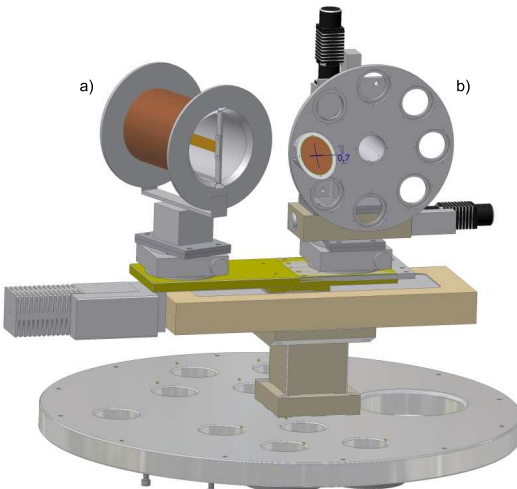


**Figure 2.4:** The goniometer holds several radiators that can be inserted onto the beam axis (b). Also available is a Møller radiator [Wall].

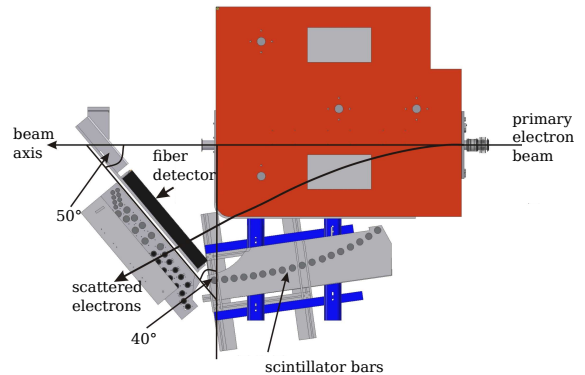


**Figure 2.5:** Top-down view of the tagging system consisting of dipole magnet (red) and scintillating bars and fibers [For10]. Electrons are deflected by the magnet after the bremsstrahlung process.

## 2.2 Liquid hydrogen target

The (polarized) photon beam impinges on a liquid hydrogen target [Ham09] which is located at the center of the crystal barrel detector, see Figure 2.1. It consists of a Kapton cell that measures 5.1 cm in length and 3 cm in diameter which is filled with liquid hydrogen. A separate cooling circuit with liquid hydrogen ensures the hydrogen that is used as target material stays liquid. Kapton is chosen as material for the target cell because the expected rate of hadronic reactions induced in the target cell is

<sup>1</sup> Hereby, the recoil energy absorbed by the nuclei is neglected.

<sup>2</sup> Full Width Half Maximum.

small compared to the expected rate from liquid hydrogen [Ham09]. Protons are bound with a binding energy of 21.4 eV in the target material, which is negligible on the scale of hadronic reaction energies, so that they can be considered free. A schematic view of the target is shown in Figure 2.6.

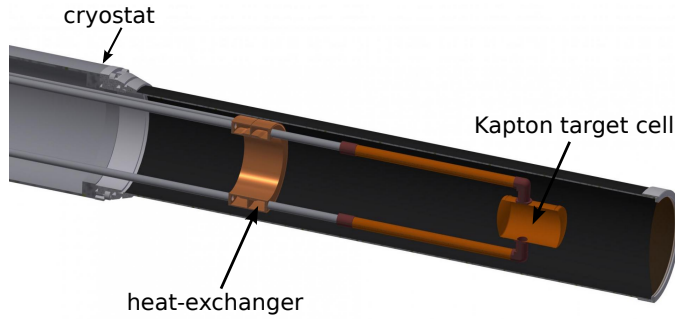


**Figure 2.6:** Schematic overview of the liquid hydrogen target. Two tubes connected to a heat exchanger and the Kapton cell allow filling it with liquid hydrogen. M. GRÜNER in [Afz19].

## 2.3 Detector system

Hadronic reactions are induced by the photon beam in the target material. As a consequence resonances are excited that decay under emission of mesons. These mesons subsequently decay to e.g. photons. The main calorimeters of the experiment, the Crystal Barrel that is complemented by the forward detector(2.3.2) and the MiniTAPS calorimeter (2.3.3), cover 95% of the solid angle  $4\pi$  and are especially suited for the detection of photons. Charged particles are identified by the inner detector (2.3.1) as well as plastic scintillators mounted in front of the forward and the MiniTAPS detector that are used as vetoes. To suppress electromagnetic reactions a ČERENKOV detector is used (2.3.4). The photon flux is measured via the Gamma-Intensity-Monitor (GIM) and Flux-Monitor (FluMo) (2.3.5).

### 2.3.1 Inner detector

The inner detector [Fös00; Suf+05] encloses the target in a cylindrical geometry and consists of 513 plastic scintillation fibers that are placed in three layers. The outer layer is oriented along the beam axis while the inner layers are tilted by an angle of  $-24.5^\circ$  and  $25.8^\circ$ , respectively, see Figure 2.7. This structure allows to determine the azimuthal and polar angle of a charged particle as long as at least two layers are hit. The detector is in total 40 cm long and covers a polar angle range of  $23.1^\circ < \theta < 166^\circ$  with a resolution of  $0.4^\circ$  in polar angle  $\theta$  and  $0.1^\circ$  in azimuthal angle  $\phi$ . The fibers consist of Polystyrene with a refractive index of  $n = 1.6$  and are cladded by Polymethylmethacrylat ( $C_5H_8O_2$ ) with  $n = 1.49$  [PDG]. Charged particles passing the detector will cause the emission of scintillation light by the Polystyrene molecules which is read out with photomultipliers after passing lightguides. Short decay times ensure a fast time signal and a time resolution of  $FWHM = (2.093 \pm 0.013)$  ns is reached [Har08].

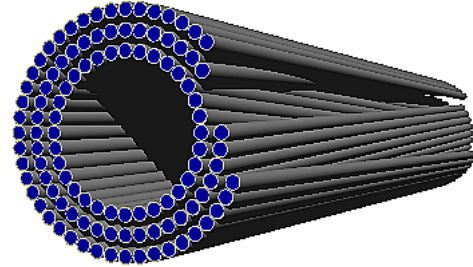


**Figure 2.7:** The inner detector with three layers of scintillating fibers. The inner two layers are tilted with respect to the outer layer. D. WALTHER in [Afz19].

### 2.3.2 Crystal Barrel and forward detector

The main calorimeter of the experiment is the Crystal Barrel detector [Ake+92]. It consists of 1320 CsI(Tl) crystals that are arranged in 24 rings facing the center of the target, see Figure 2.8. The first

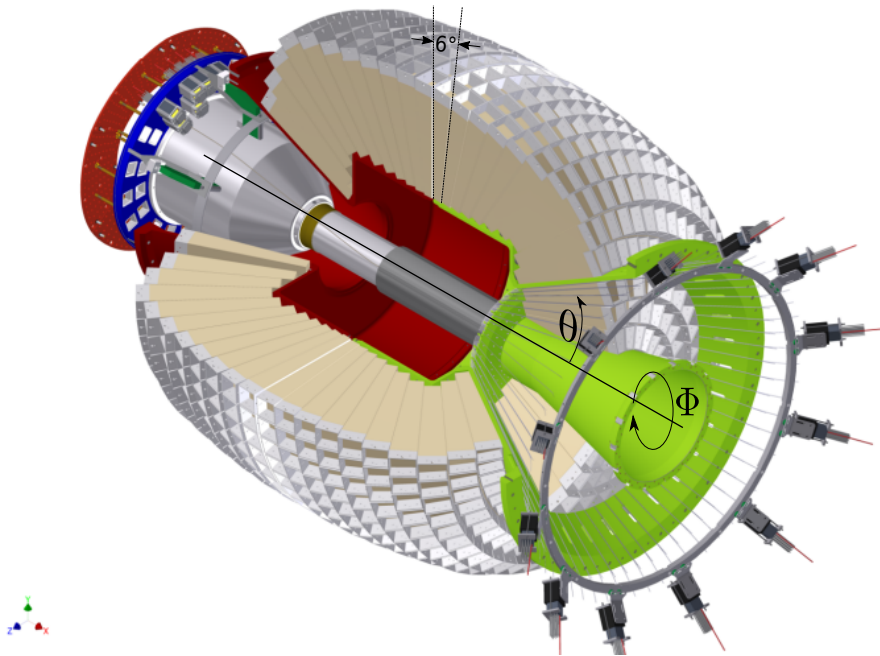


**Figure 2.8:** Crystal barrel calorimeter and forward detector are built such that they enclose the target and the inner detector. The forward detector consists of the first three rings (green base) of crystals which are additionally covered by plastic scintillators for charged particle identification. The definition of polar angle  $\theta$  and azimuthal angle  $\phi$  in the LAB system are indicated as well. D. WALTHER in [Urb17]

three rings in forward direction contain 30 crystals each and build the forward detector, covering the polar angle range  $11.18^\circ < \theta < 27.54^\circ$ . Also the 24<sup>th</sup> ring contains 30 crystals, all other rings are made up of 60 crystals. The crystals are shaped like truncated trapezoidal pyramids that cover 6° in

polar angle  $\theta$  and azimuthal angle  $\phi$ . Only in the first three and the last ring the crystals cover  $12^\circ$  in  $\phi$ . Full coverage in  $\phi$  and 80% ( $12^\circ < \theta < 156^\circ$ ) coverage in  $\theta$  are achieved by the forward detector and the Crystal Barrel. Photons from neutral mesonic decays are very high energetic and will interact with the inorganic scintillator material mainly via pair production [Leo94]. The produced electrons and positrons will themselves interact mainly via bremsstrahlung such that usually an electromagnetic shower is created upon photon impact that may spread over several crystals. Using crystals with a length of  $l = 30$  cm photons with an energy of up to 2 GeV may deposit their entire energy in the calorimeter since the  $l$  corresponds to 16.22 radiation lengths  $X_0$  [Ake+92]. The transversal spread of a shower is given by the MÓLIERE radius which is 3.8 cm for CsI(Tl) [Ake+92]. By determining the focal point of the electromagnetic showers an angular resolution of less than  $2^\circ$  can be achieved [Jun04] while the energy resolution is given by [Ake+92]

$$\frac{\sigma_E}{E} = \frac{2.5\%}{\sqrt[4]{E/\text{GeV}}}, \quad (2.3)$$

depending on the initial photon energy  $E$ . The energy loss of heavier charged particles, e.g. a proton, is described by the BETHE-BLOCH formula [Bet30]. Depending on their mass they only deposit their full energy up to a certain threshold energy above which they are characterized as Minimal Ionizing Particles (MIP).

The emitted scintillation light of crystals not belonging to the forward detector is read out using PIN photodiodes. A wavelength shifter ensures meeting the sensitive spectral range of the photodiodes. The long decay times of the scintillation light and the slow preamplifiers following the photodiodes do not allow the determination of a timing information for particles detected in the Crystal Barrel<sup>3</sup>, so that the Crystal Barrel is optimized for energy measurements.

Crystals belonging to the forward detector are read out using Photomultipliers. They provide a faster signal, such that timing information for forward detector hits is available with a time resolution of FWHM =  $(1.861 \pm 0.016)$  ns [Har08]. Additionally plastic scintillator plates are mounted in front [Wen04], allowing the identification of charged particles with an efficiency of 72% [Geh15]. Optical fibers guide the scintillation light from the plates to photomultipliers.

### 2.3.3 MiniTAPS

Since the Crystal Barrel only covers the solid angle starting at  $\theta \approx 12^\circ$ . It is supplemented by the Mini-Two-Arm-Photon-Spectrometer (MiniTAPS) [Gab+94; Str96] for polar angles  $1^\circ < \theta < 12^\circ$ . The MiniTAPS detector is placed in a distance of  $d = 2.1$  m from the target and consists of 216 hexagonally shaped BaF<sub>2</sub> crystals, see Figure 2.9. Each crystal has a length of  $l = 25$  cm which is equivalent to 12 radiation lengths [Nov91] and a width of  $w = 5.8$  cm. The chosen material has a high density and is able to withstand high reaction rates [PDG]. This is important here because most reactions will be strongly boosted in forward direction towards small  $\theta$ . Different mechanisms of scintillation allow to extract a fast and a slow component [Leo94] which are read out using photomultipliers and separately used for timing and energy information, respectively. Hereby a time

---

<sup>3</sup> As of 2014, the PIN photodiodes have been replaced by avalanche photodiodes (APD) [Hon14; Urb17], allowing a fast read out that can be used to provide timing information and also as part of the trigger.

resolution of  $\text{FWHM} = (0.872 \pm 0.006)$  ns [Har08] and an energy resolution of [Gab+94]

$$\frac{\sigma_E}{E} = 1.9\% + 0.59\% \cdot \sqrt{E/\text{GeV}} \quad (2.4)$$

is achieved. At the same time an angular precision of  $0.2^\circ$  in  $\theta$  is reached.

In front of each  $\text{BaF}_2$  crystal, plastic scintillator plates are mounted to identify charged particles. Their scintillation light is guided towards photomultipliers using optical fibers. With these scintillators a time resolution of  $\text{FWHM} = (3.06 \pm 0.05)$  ns is obtained [Har08].

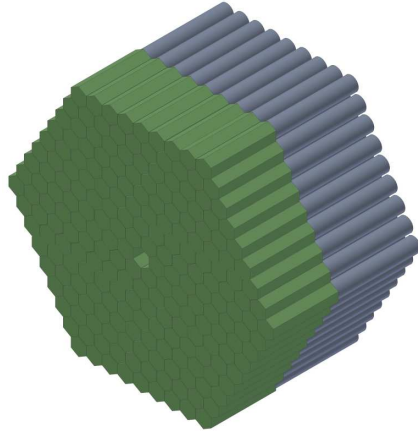


**Figure 2.9:** The MiniTAPS detector is made up of 216  $\text{BaF}_2$  crystals (grey). In front of each crystal, plastic scintillators are mounted for charged particle information. Taken from [Wal].

### 2.3.4 ČERENKOV detector

When the photon beam impinges on the proton target, not only hadronic reactions are induced but also electromagnetic reactions. Because the beam energy is very high on the scale of electromagnetic interactions, any produced electrons and positrons are highly relativistic and boosted to small polar angles. To suppress these events already during data acquisition a ČERENKOV detector [Kai07] is positioned between the MiniTAPS calorimeter and the Crystal Barrel, see Figure 2.1. It is filled with  $\text{CO}_2$  gas where ČERENKOV light is emitted by electrons or positrons above an energy of 17.4 MeV. This follows from the refractive index which is given as  $n_{\text{CO}_2} = 1.00045$  [PDG]. The emitted ČERENKOV radiation is focused on a photodiode using a parabolic mirror. The presence of a signal can then be used as veto during data acquisition to reduce the amount of recorded electromagnetic background. Electrons and positrons are detected with an efficiency of up to  $(99.72 \pm 0.45)\%$  [Kai07].

### 2.3.5 Flux monitoring

The FluMo and GIM detector are used to determine the total number of photons incident on the target and are located behind the MiniTAPS detector, as is shown in Figure 2.1.

The GIM detector [McG08] is made of 16  $\text{PbF}_2$  crystals placed in a  $4 \times 4$  array, see Figure 2.10. Incoming photons will interact with the material mainly via pair production [Leo94]. The produced electrons and positrons are highly relativistic and will emit ČERENKOV light that is collected

with photomultipliers. For reaction rates higher than 5 MHz the GIM detector efficiency decreases significantly. For rates above 7 MHz more than 10% of events are not registered [Har08]. To

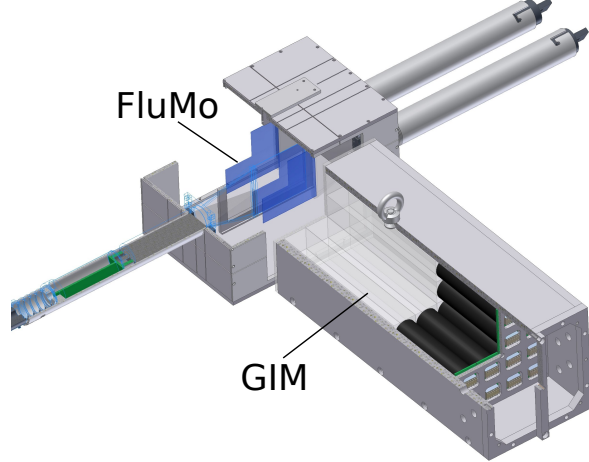


**Figure 2.10:** The two detectors FluMo and GIM are used to monitor the photon flux at different reaction rates. D. WALTHER in [Afz19].

compensate this the FluMo detector [Die08] is used as soon as deadtime effects influence the performance of the GIM detector. A converter plate made of lead, two scintillators and a veto detector are part of the FluMo detector. Impinging photons may create electron positron pairs that are detected in a coincidence measurement using the two scintillators. A plastic scintillation detector is placed before the converter plate and gives a veto signal if charged particles pass through it.

## 2.4 Trigger

## 2.5 Software and Monte Carlo

## 2.6 Datasets



# Bibliography

---

- [Wor+22] R. L. Workman et al., *Review of Particle Physics*, PTEP **2022** (2022) 083C01 (cit. on pp. 2, 3, 17–19, 22, 24, 32, 79, 81).
- [LMP01] U. Löring, B. Metsch and H. Petry, *The light-baryon spectrum in a relativistic quark model with instanton-induced quark forces*, The European Physical Journal A **10** (2001) 395, issn: 1434-601X, URL: <http://dx.doi.org/10.1007/s100500170105> (cit. on pp. 2, 3).
- [KS03] B. Krusche and S. Schadmand, *Study of nonstrange baryon resonances with meson photoproduction*, Prog. Part. Nucl. Phys. **51** (2003) 399, arXiv: nucl-ex/0306023 (cit. on pp. 3, 4).
- [Afz19] F. N. Afzal, *Measurement of the beam and helicity asymmetries in the reactions  $\gamma p \rightarrow p\pi^0$  and  $\gamma p \rightarrow p\eta$* , PhD thesis: Rheinische Friedrich-Wilhelms-Universität Bonn, 2019, URL: <https://hdl.handle.net/20.500.11811/8064> (cit. on pp. 4, 7, 9, 11, 12, 15, 17, 27, 29, 41, 42, 44, 45, 49, 50, 54, 55, 59, 62, 65, 66, 74, 76, 79, 83).
- [DT92] D. Drechsel and L. Tiator, *Threshold pion photoproduction on nucleons*, J. Phys. G **18** (1992) 449 (cit. on p. 4).
- [Bar+18] M. Bartelmann et al., *Theoretische Physik 3 — Quantenmechanik*, 2018, ISBN: 978-3-662-56071-6 (cit. on p. 4).
- [Bar89] R. J. Barlow, *Statistics, A Guide to the Use of Statistical Methods in the Physical Sciences*, Wiley, 1989 (cit. on pp. 5, 45, 46, 51).
- [Leo94] W. R. Leo, *Techniques for Nuclear and Particle Physics Experiments, A How-to Approach*, vol. 2, Springer-Verlag Berlin Heidelberg GmbH, 1994 (cit. on pp. 8, 13, 14, 79).
- [Hei54] W. Heitler, *The Quantum Theory of Radiation*, Oxford University Press, 1954 (cit. on p. 8).
- [Dem10] W. Demtröder, *Experimentalphysik 3, Atome, Moleküle, Festkörper*, vol. 4, Springer-Verlag Berlin Heidelberg New York, 2010 (cit. on p. 8).
- [Nat+03] F. Natter, P. Grabmayr, T. Hehl, R. Owens and S. Wunderlich, *Monte Carlo simulation and analytical calculation of coherent bremsstrahlung and its polarisation*, Nuclear Instruments and Methods in Physics Research Section B: Beam Interactions with Materials and Atoms **211** (2003) 465 (cit. on p. 9).

## Bibliography

---

- [Els+09] D. Elsner et al., *Linearly polarised photon beams at ELSA and measurement of the beam asymmetry in  $\pi^0$  photoproduction off the proton*, The European Physical Journal A **39** (2009) 373, URL: <https://doi.org/10.1140%2Fepja%2F12008-10708-1> (cit. on p. 9).
- [Kam10] S. Kammer, *Strahlpolarimetrie am CBELSA/TAPS Experiment*, PhD thesis: Rheinische Friedrich-Wilhelms-Universität Bonn, 2010, URL: <https://hdl.handle.net/20.500.11811/4539> (cit. on p. 9).
- [For10] K. Fornet-Ponse, *Die Photonenmarkierungsanlage für das Crystal-Barrel/TAPS-Experiment an ELSA*, PhD thesis: Rheinische Friedrich-Wilhelms-Universität Bonn, 2010, URL: <https://hdl.handle.net/20.500.11811/4507> (cit. on p. 10).
- [Har08] J. Hartmann, *Zeitkalibrierung und Photonenflussbestimmung für das Crystal-Barrel-Experiment and ELSA*, Diploma thesis: Rheinische Friedrich-Wilhelms-Universität Bonn, 2008 (cit. on pp. 10, 11, 13–15).
- [Wal] D. Walther, *Crystal Barrel, A  $4\pi$  photon spectrometer*, URL: <https://www.cb.uni-bonn.de> (visited on 27/09/2021) (cit. on pp. 10, 14).
- [Ham09] C. Hammann, *Aufbau eines Flüssigwasserstofftargets zur Durchführung von Kalibrationsmessungen am Crystal-Barrel Experiment an ELSA*, Diploma thesis: Rheinische Friedrich-Wilhelms-Universität Bonn, 2009 (cit. on pp. 10, 11).
- [Fös00] A. Fösel, *Entwicklung und Bau des Innendetektors für das Crystal Barrel Experiment an ELSA/Bonn*, PhD thesis: Friedrich-Alexander-Universität Erlangen-Nürnberg, 2000 (cit. on p. 11).
- [Suf+05] G. Suft et al., *A scintillating fibre detector for the Crystal Barrel experiment at ELSA*, Nucl. Instrum. Meth. A **538** (2005) 416 (cit. on p. 11).
- [PDG] PDG, *Atomic and Nuclear Properties*, URL: <https://pdg.lbl.gov/2022/AtomicNuclearProperties/index.html> (visited on 04/08/2022) (cit. on pp. 11, 13, 14).
- [Ake+92] E. Aker et al., *The Crystal Barrel spectrometer at LEAR*, Nucl. Instrum. Meth. A **321** (1992) 69 (cit. on pp. 12, 13).
- [Urb17] M. Urban, *Design eines neuen Lichtpulsersystems sowie Aufbau und Inbetriebnahme der neuen APD Auslese für das Crystal-Barrel-Kalorimeter*, PhD thesis: Rheinische Friedrich-Wilhelms-Universität Bonn, 2017 (cit. on pp. 12, 13, 18).
- [Jun04] J. Junkersfeld, *Kalibration des Crystal-Barrel-ELSA Detektors mit Hilfe der Reaktion  $\gamma p \rightarrow p\pi^0$* , Diploma thesis: Rheinische Friedrich-Wilhelms-Universität Bonn, 2004 (cit. on p. 13).

- 
- [Bet30] H. Bethe, *Zur Theorie des Durchgangs schneller Korpuskularstrahlen durch Materie*, Annalen der Physik **397** (1930) 325, eprint:  
<https://onlinelibrary.wiley.com/doi/pdf/10.1002/andp.19303970303>,  
URL:  
<https://onlinelibrary.wiley.com/doi/abs/10.1002/andp.19303970303>  
(cit. on p. 13).
- [Hon14] C. Honisch, *Design, Aufbau und Test einer neuen Ausleseelektronik für das Crystal-Barrel-Kalorimeter*,  
PhD thesis: Rheinische Friedrich-Wilhelms-Universität Bonn, 2014 (cit. on p. 13).
- [Wen04] C. Wendel, *Entwicklung eines Szintillations-Detektors zur Identifikation geladener Teilchen im Crystal-Barrel Vorwärtsdetektor*,  
Diploma thesis: Rheinische Friedrich-Wilhelms-Universität Bonn, 2004 (cit. on p. 13).
- [Geh15] S. Gehring, *Test des Szintillationsdetektors zur Identifikation geladener Teilchen im Crystal-Barrel-Vorwärtsdetektor*,  
Bachelor thesis: Rheinische Friedrich-Wilhelms-Universität Bonn, 2015 (cit. on p. 13).
- [Gab+94] A. Gabler et al.,  
*Response of TAPS to monochromatic photons with energies between 45 and 790 MeV*,  
Nuclear Instruments and Methods in Physics Research Section A: Accelerators,  
Spectrometers, Detectors and Associated Equipment **346** (1994) 168, ISSN: 0168-9002,  
URL:  
<https://www.sciencedirect.com/science/article/pii/0168900294907013>  
(cit. on pp. 13, 14).
- [Str96] H. Ströher, *Electromagnetic and Hadronic Probes of Nuclear Matter: Portrait of the European Photon Detector TAPS*, Nuclear Physics News **6** (1996) 7,  
eprint: <https://doi.org/10.1080/10506899609411060>,  
URL: <https://doi.org/10.1080/10506899609411060> (cit. on p. 13).
- [Nov91] R. Novotny, *The BaF/sub 2/ photon spectrometer TAPS*,  
IEEE Transactions on Nuclear Science **38** (1991) 379 (cit. on p. 13).
- [Kai07] D. Kaiser,  
*Aufbau und Test des Gas- Čerenkov-Detektors für den Crystal-Barrel-Aufbau an ELSA*,  
Diploma thesis: Rheinische Friedrich-Wilhelms-Universität Bonn, 2007 (cit. on p. 14).
- [McG08] W. McGehee, *The Gamma Intensity Monitor of the Crystal-Barrel-Experiment*,  
Bachelor thesis: Massachusetts Institute of Technology, 2008 (cit. on p. 14).
- [Die08] J. Dielmann, *Entwicklung, Aufbau und Test eines Detektors zur Bestimmung des Photonenflusses an der Bonner Photonenmarkierungsanlage*,  
Diploma thesis: Rheinische Friedrich-Wilhelms-Universität Bonn, 2008 (cit. on p. 15).
- [Afz12] F. N. Afzal, *Analysis of Crystal Barrel Data - Measurement of the double polarization observable E in the reaction  $\vec{\gamma}p \rightarrow \eta' p$* ,  
Master thesis: Rheinische Friedrich-Wilhelms-Universität Bonn, 2012 (cit. on p. 17).
- [Dah08] T. Dahlke, *Bestimmung einer winkelabhängigen Energiekorrekturfunktion für das TAPS-Kalorimeter des Crystal-Barrel/TAPS-Experiments and ELSA*,  
Diploma thesis: Rheinische Friedrich-Wilhelms-Universität Bonn, 2008 (cit. on p. 18).

## Bibliography

---

- [GP08] M. Grüner and D.-M. Piontek, *Hit reconstruction in ChaPI*, CB-TR16 Note 003 (2008) (cit. on p. 18).
- [Ike+00] H. Ikeda et al., *A detailed test of the CsI(Tl) calorimeter for BELLE with photon beams of energy between 20-MeV and 5.4-GeV*, Nucl. Instrum. Meth. A **441** (2000) 401 (cit. on pp. 24, 26).
- [Cre+09] V. Crede et al., *Photoproduction of eta and eta-prime mesons off protons*, Phys. Rev. C **80** (2009) 055202, arXiv: [0909.1248](https://arxiv.org/abs/0909.1248) [nucl-ex] (cit. on pp. 24, 29, 32).
- [Har17] J. Hartmann, *Measurement of Double Polarization Observables in the Reactions  $\gamma p \rightarrow p\pi^0$  and  $\gamma p \rightarrow p\eta$  with the Crystal Barrel/TAPS Experiment at ELSA*, PhD thesis: Rheinische Friedrich-Wilhelms-Universität Bonn, 2017, URL: <https://hdl.handle.net/20.500.11811/7258> (cit. on pp. 29, 47, 49).
- [Die+20] M. Dieterle et al., *Helicity-Dependent Cross Sections for the Photoproduction of  $\pi^0$  Pairs from Nucleons*, Physical Review Letters **125** (2020), URL: <https://doi.org/10.1103/PhysRevLett.125.062001> (cit. on p. 32).
- [Käs+18] A. Käser et al., *First measurement of helicity-dependent cross sections in  $\pi^0\eta$  photoproduction from quasi-free nucleons*, Physics Letters B **786** (2018) 305, URL: <https://doi.org/10.1016/j.physletb.2018.10.006> (cit. on p. 32).
- [Bar+05] O. Bartholomy et al., *Neutral-Pion Photoproduction off Protons in the Energy Range  $0.3 \text{ GeV} < E_\gamma < 3 \text{ GeV}$* , Physical Review Letters **94** (2005), URL: <https://doi.org/10.1103/PhysRevLett.94.012003> (cit. on p. 32).
- [Sta+11] A. Starostin et al., *Measurement of  $3\pi^0$  photoproduction on the proton from threshold to 1.4 GeV*, 2011, URL: <https://arxiv.org/abs/1101.3744> (cit. on p. 32).
- [Mur+20] N. Muramatsu et al., *Differential cross sections, photon beam asymmetries, and spin density matrix elements of  $\omega$  photoproduction off the proton at  $E_\gamma = 1.3 - 2.4 \text{ GeV}$* , Phys. Rev. C **102** (2 2020) 025201, URL: <https://link.aps.org/doi/10.1103/PhysRevC.102.025201> (cit. on p. 32).
- [Str+76] W. Struczinski et al., *Study of photoproduction on hydrogen in a streamer chamber with tagged photons for  $1.6 \text{ GeV} < E_\gamma < 6.3 \text{ GeV}$ . Topological and reaction cross sections*, Nuclear Physics B **108** (1976) 45, ISSN: 0550-3213, URL: <https://www.sciencedirect.com/science/article/pii/0550321376901231> (cit. on p. 32).
- [Dug+09] M. Dugger et al.,  *$\pi^+$  photoproduction on the proton for photon energies from 0.725 to 2.875 GeV*, Physical Review C **79** (2009), URL: <https://doi.org/10.1103/PhysRevC.79.065206> (cit. on p. 32).
- [Mah22] P. Mahlberg, *Thesis in Preparation*, Rheinische Friedrich-Wilhelms-Universität Bonn, 2022 (cit. on pp. 40, 72, 74).

- 
- [San+11] A. M. Sandorfi, S. Hoblit, H. Kamano and T.-S. H. Lee, *Determining pseudoscalar meson photoproduction amplitudes from complete experiments*, Journal of Physics G: Nuclear and Particle Physics **38** (2011) 053001, issn: 1361-6471, url: <http://dx.doi.org/10.1088/0954-3899/38/5/053001> (cit. on p. 43).
- [Afz+20] F. Afzal et al.,  
*Observation of the  $p\eta'$  Cusp in the New Precise Beam Asymmetry  $\Sigma$  Data for  $\gamma p \rightarrow p\eta$* , Phys. Rev. Lett. **125** (15 2020) 152002,  
url: <https://link.aps.org/doi/10.1103/PhysRevLett.125.152002> (cit. on pp. 44, 83).
- [Pov+14] B. Povh, K. Rith, C. Scholz, F. Zetsche and W. Rodejohann,  
*Teilchen und Kerne, Eine Einführung in die physikalischen Konzepte*, vol. 9, Springer Spektrum, 2014 (cit. on p. 45).
- [RP22] G. van Rossum and the Python development team,  
*The Python Language Reference, Release 3.10.5*, 2022,  
url: <https://docs.python.org/3.10/reference/index.html> (cit. on pp. 46, 62).
- [Vir+20] P. Virtanen et al., *SciPy 1.0: Fundamental Algorithms for Scientific Computing in Python*, Nature Methods **17** (2020) 261 (cit. on p. 46).
- [BR97] R. Brun and F. Rademakers, *ROOT — An object oriented data analysis framework*, Nucl. Instrum. Meth. A **389** (1997) 81, issn: 0168-9002, url: <https://www.sciencedirect.com/science/article/pii/S016890029700048X> (cit. on pp. 46, 49, 50, 62).
- [sci] *scipy, scipy.optimize.curve\_fit, Function Documentation*,  
url: [https://docs.scipy.org/doc/scipy/reference/generated/scipy.optimize.curve\\_fit.html](https://docs.scipy.org/doc/scipy/reference/generated/scipy.optimize.curve_fit.html) (visited on 28/06/2022) (cit. on p. 46).
- [ROOa] ROOT, *TH1 Class reference*, url: <https://root.cern.ch/doc/master/classTH1.html#a63eb028df86bc86c8e20c989eb23fb2a> (visited on 28/06/2022) (cit. on p. 46).
- [Gel+14] A. Gelman et al., *Bayesian Data Analysis*, vol. 3, Chapman & Hall/CRC, 2014 (cit. on p. 46).
- [Sta22a] Stan development team, *Prior Choice Recommendations*, 2022, url: <https://github.com/stan-dev/stan/wiki/Prior-Choice-Recommendations> (visited on 02/07/2022) (cit. on p. 46).
- [Sta22b] Stan development team, *Stan Modeling Language Users Guide and Reference Manual*, vol. 2.29, 2022, url: <https://mc-stan.org> (cit. on pp. 46, 49, 62, 67, 70, 83).
- [HG14] M. D. Hoffman and A. Gelman,  
*The No-U-Turn Sampler: Adaptively Setting Path Lengths in Hamiltonian Monte Carlo*, Journal of Machine Learning Research **15** (2014) 1593,  
url: <http://jmlr.org/papers/v15/hoffman14a.html> (cit. on pp. 46, 49).

## Bibliography

---

- [ROOb] ROOT, *TTree Class reference*, URL: <https://root.cern.ch/doc/master/classTTree.html#a3e6bf252ab8653b47cc9116950f3ee7b> (visited on 28/06/2022) (cit. on p. 49).
- [JR75] F. James and M. Roos, *Minuit - a system for function minimization and analysis of the parameter errors and correlations*, Computer Physics Communications **10** (1975) 343, ISSN: 0010-4655, URL: <https://www.sciencedirect.com/science/article/pii/0010465575900399> (cit. on p. 49).
- [ROOc] ROOT, *TF1 Class reference*, URL: <https://root.cern.ch/doc/master/classTF1.html#a410b0219e18e80d3e305b4d97374c077> (visited on 28/06/2022) (cit. on p. 50).
- [Veh+19] A. Vehtari, A. Gelman, D. Simpson, B. Carpenter and P.-C. Bürkner, *Rank-normalization, folding, and localization: An improved  $\hat{R}$  for assessing convergence of MCMC*, arXiv e-prints, arXiv:1903.08008 (2019) arXiv:1903.08008, arXiv: 1903.08008 [stat.CO] (cit. on p. 54).
- [Lev+14] P. Levi Sandri et al., *First Measurement of the  $\Sigma$  Beam Asymmetry in  $\eta'$  Photoproduction off the Proton near Threshold*, (2014) (cit. on pp. 79, 81).
- [Col+17] P. Collins et al., *Photon beam asymmetry  $\Sigma$  for  $\eta$  and  $\eta'$  photoproduction from the proton*, Physics Letters B (2017) (cit. on pp. 79–81).
- [Tia+18] L. Tiator et al., *Eta and etaprime photoproduction on the nucleon with the isobar model EtaMAID2018*, The European Physical Journal A **54** (2018), URL: <https://doi.org/10.1140%2Fepja%2F2018-12643-x> (cit. on pp. 81, 82).

# List of Figures

---

1.1	Running coupling of QCD. The colored data points represent different methods to obtain a value for $\alpha_s$ . For more details it may be referred to [Wor+22]. . . . .	2
1.2	Calculated nucleon (isospin $I = 1/2$ ) resonances compared to measurements. Left in each column are the calculations [LMP01], the middle shows the measurements and PDG rating [Wor+22] . . . . .	3
1.3	FEYNMAN diagram for the s-channel photoproduction of pseudoscalar mesons, adapted from [Afz19] . . . . .	4
2.1	Overview of the experimental hall of the CBELSA/TAPS experiment. The electron beam from ELSA enters at the top right. M. GRÜNER in [Afz19] . . . . .	7
2.2	Illustration of the bremsstrahlung process: An electron $e^-$ is deflected in the COLOUMB field of a nucleus in the radiator material. A photon $\gamma$ is emitted and so the momentum $q$ is transferred. . . . .	8
2.3	Left: Incoherent (green) and crystal (blue) bremsstrahlung intensities as a function of the photon energy. Right: The enhancement spectrum is given as the ratio of crystal to incoherent intensity spectrum. The dashed line at the bottom shows the calculated polarization degree. Both spectra are generated using ANB calculations. Taken from [Afz19]. . . . .	9
2.4	The goniometer holds several radiators that can be inserted onto the beam axis (b). Also available is a MØLLER radiator [Wal]. . . . .	10
2.5	Top-down view of the tagging system consisting of dipole magnet (red) and scintillating bars and fibers [For10]. Electrons are deflected by the magnet after the bremsstrahlung process. . . . .	10
2.6	Schematic overview of the liquid hydrogen target. Two tubes connected to a heat exchanger and the Kapton cell allow filling it with liquid hydrogen. M. GRÜNER in [Afz19]. . . . .	11
2.7	The inner detector with three layers of scintillating fibers. The inner two layers are tilted with respect to the outer layer. D. WALTHER in [Afz19]. . . . .	12
2.8	Crystal barrel calorimeter and forward detector are built such that they enclose the target and the inner detector. The forward detector consists of the first three rings (green base) of crystals which are additionally covered by plastic scintillators for charged particle identification. The definition of polar angle $\theta$ and azimuthal angle $\phi$ in the LAB system are indicated as well.D. WALTHER in [Urb17] . . . . .	12
2.9	The MiniTAPS detector is made up of 216 BaF <sub>2</sub> crystals (grey). In front of each crystal, plastic scintillators are mounted for charged particle information. Taken from [Wal]. . . . .	14

2.10	The two detectors FluMo and GIM are used to monitor the photon flux at different reaction rates. D. WALTHER in [Afz19]. . . . .	15
3.1	Distribution of event classes in $\eta' \rightarrow \gamma\gamma$ production . . . . .	19
3.2	Time information of all final state particles and the beam photon for 3PED $\eta'$ production . . . . .	20
3.3	Reaction time $t_r$ for 3PED and 2.5PED $\eta'$ production. The yellow region indicate the sidebands while the purple colored interval is the selected prompt peak. . . . .	21
3.4	Coplanarity of the $p\eta'$ final state with all other cuts applied for the energy bin $1500 \text{ MeV} \leq E_\gamma < 1600 \text{ MeV}$ . The vertical dashed lines show the cut ranges obtained from a gaussian fit to the data (open circles). The solid black histograms represent fitted MC data of $\eta' \rightarrow \gamma\gamma$ . . . . .	25
3.5	Polar angle difference of the $p\eta'$ final state with all other cuts applied for the energy bin $1500 \text{ MeV} \leq E_\gamma < 1600 \text{ MeV}$ . The vertical dashed lines show the cut ranges obtained from a gaussian fit to the data (open circles). The solid black histograms represent fitted MC data of $\eta' \rightarrow \gamma\gamma$ . . . . .	26
3.6	Missing mass of the $p\eta'$ final state with all other cuts applied for the energy bin $1500 \text{ MeV} \leq E_\gamma < 1600 \text{ MeV}$ . The vertical dashed lines show the cut ranges obtained from a fit to data (open circles) employing a Novosibirsk function. The solid colored histograms represent fitted MC data from relevant photoproduction reactions: in black $\eta'$ , in green $\pi^0$ , in red $\eta$ , in blue $\omega$ , in yellow $2\pi^0$ , magenta $\pi^0\eta$ . The turquoise histogram is the sum of all MC histograms. . . . .	27
3.7	Invariant mass of the $p\eta'$ final state with all other cuts applied for all energy and angular bins. The open circles represent the measured data, the solid colored histograms fitted MC data from relevant photoproduction reactions: in black $\eta'$ , in green $\pi^0$ , in red $\eta$ , in blue $\omega$ , in yellow $2\pi^0$ and in magenta $\pi^0\eta$ . The turquoise histogram is the sum of all MC histograms. . . . .	28
3.8	Invariant mass of the $p\eta'$ final state with all other cuts applied for the energy bin $1500 \text{ MeV} \leq E_\gamma < 1600 \text{ MeV}$ . The vertical dashed lines show the cut ranges obtained from a gaussian fit to the $\eta'$ MC data (solid black histogram). The open circles represent the measured data, the solid colored histograms fitted MC data from relevant photoproduction reactions: in black $\eta'$ , in green $\pi^0$ , in red $\eta$ , in blue $\omega$ , in yellow $2\pi^0$ and in magenta $\pi^0\eta$ . The turquoise histogram is the sum of all MC histograms. . . . .	28
3.9	Acceptance for the reaction $\gamma p \rightarrow p\eta'$ after all cuts that have been discussed so far for 2.5PED and 3PED events . . . . .	29
3.10	Fraction of background events in the analyzed beam energy and angular bins. . . . .	30
3.11	Acceptance for possible background contributions . . . . .	31
3.12	Generated energies of $\gamma_3$ and $\gamma_4$ in $2\pi^0$ and $\pi^0\eta$ photoproduction MC data. The threshold of 20 MeV is marked by a vertical red line. $E_{\gamma_4}$ is shown on the top, $E_{\gamma_3}$ is shown on the bottom of each figure. . . . .	33
3.13	$E_\gamma^{\text{gen}}$ vs. $E_\gamma^{\text{rec}}$ of $\gamma_1$ and $\gamma_2$ for $2\pi^0$ (top) and $\pi^0\eta$ (bottom) production. The slope $E_\gamma^{\text{gen}} = E_\gamma^{\text{rec}}$ is marked by a solid line. . . . .	35
3.14	Polar angle difference $\Delta\theta$ between $\gamma_2$ and $\gamma_3$ of the $\pi^0\eta$ final state. . . . .	36
3.15	Illustration of the misidentification process during reconstruction. Enumeration of photons is now arbitrary. . . . .	36

3.16 Generated CMS angle $\cos \theta_{\text{gen.}}$ vs. reconstructed CMS angle $\cos \theta_{\text{rec.}}$ for both background reactions. The slope $\cos \theta_{\text{gen.}} = \cos \theta_{\text{rec.}}$ is indicated by the solid line. . . . .	37
3.17 Detector hits of the recoil proton, as obtained from MC data for the production of $\eta'$ , $2\pi^0$ and $\pi^0\eta$ . CB: Crystal Barrel, FW: forward dector, MT: MiniTAPS . . . . .	39
3.18 Difference in measured and calculated beam energy. Data points are shown as open circles, MC data as solid histograms: in black $\eta'$ , in green $\pi^0$ , in red $\eta$ , in blue $\omega$ , in yellow $2\pi^0$ and in magenta $\pi^0\eta$ . The turquoise histogram is the sum of all MC histograms. . . . .	40
3.19 Invariant mass spectrum passing different stages in the event selection process. In the end clear peaks for all possibly produced mesons are visible. The vertical lines indicate the mean cut ranges over all energy and angle bins. . . . .	41
3.20 Invariant mass spectrum passing different stages in the event selection process. In the end clear peaks for all possibly produced mesons are visible. Taken from [Afz19]. . .	42
4.1 Left: Definition of angles $\alpha, \phi, \varphi$ . Right: Photon momentum $\vec{k}$ and polarization $\vec{\epsilon}$ define the beam polarization plane while the reaction plane is defined by the recoil proton $p$ and produced meson $M$ . . . . .	43
4.2 Posterior predictive checks $p(A_{\text{rep}} A)$ from a BAYESIAN fit to the event yield asymmetries for six toy Monte Carlo bins are shown as distributions. The data points in the upper plot are the asymmetry $A(\phi)$ , which was additionally fitted using a $\chi^2$ fit (solid line). The goodness of fit is shown using $p$ -values, which give the fraction $T(A_{\text{rep}} > A)$ of replicated samples greater than the original measured value, with propagated statistical error bars on the bottom of each plot. The expected mean value of $T(A_{\text{rep}} > A) = 0.5$ is indicated by the dashed line. . . . .	52
4.3 $p$ values of all toy Monte Carlo bins. They are centered around their mean at 0.5, which is indicated by the dashed line, and show no bias towards higher or lower values, thus confirming an adequate fit. . . . .	53
4.4 Left: Combined posterior distributions of all 10000 fits normalized by their respective standard deviation. Right: Unaltered combined posterior distributions of all 10000 fits. A GAUSSIAN fit was performed to determine mean $\mu$ and standard deviation $\sigma$ of the distributions with results given on top. . . . .	53
4.5 Left: relative error $\frac{\sigma_{\text{MCSE}}}{\text{median}[P(\Sigma y)]}$ Right: $\widehat{R}$ associated with the fit parameter $\Sigma$ . Both are shown for all 10000 fits. The critical values that should not be exceeded are marked by dashed lines. . . . .	54
4.6 Combined posteriors for the beam asymmetries $\Sigma$ and $\Sigma^{\text{bkg}}$ from all 1000 event based fits. Left: Residuals $\Xi$ Right: Unnormalized posterior distributions. A GAUSSIAN fit is performed on the distributions with results for mean $\mu$ and standard deviation $\sigma$ on top. . . . .	56
4.7 Combined posterior probabilities using the <i>pooled likelihood</i> approach. Left: Signal beam asymmetry, Right: background beam asymmetry. Mean and standard deviation as obtained from a Gaussian fit are shown on top . . . . .	57
4.8 Left: relative error $\frac{\sigma_{\text{MCSE}}}{\text{median}[P(\Sigma y)]}$ Right: $\widehat{R}$ associated with the fit parameter $\Sigma$ . Both are shown for all 1000 fits. The critical values that should not be exceeded are marked by dashed lines. . . . .	57

4.9	Posterior predictive check using the draws of the detector coefficients $a$ and $b$ . Points with error bars are the polarization weighted sum of event yields. The dashed line is the mean of the predictive values while the solid opaque lines are representative of one simulation draw $a^{(s)}, b^{(s)}$ . . . . .	58
4.10	Posterior predictive checks $p(A_{\text{rep}} A)$ from a BAYESIAN fit to the event yield asymmetries for all angular bins of the energy bin $1250 \text{ MeV} \leq E_\gamma < 1310 \text{ MeV}$ . The data points in the upper plot are the asymmetry $A(\phi)$ , which was additionally fitted using a $\chi^2$ fit (solid line). The goodness of fit is shown using $p$ -values, which give the fraction $T(A_{\text{rep}} > A)$ of replicated samples greater than the original measured value, with propagated statistical error bars on the bottom of each plot. The expected mean value of $T(A_{\text{rep}} > A) = 0.5$ is indicated by the dashed line. . . . .	60
4.11	$p$ values generated using all fits. They are centered around their mean at 0.5, which is indicated by the dashed line, and show no bias towards higher or lower values, thus confirming an adequate fit. . . . .	61
4.12	Left: relative error $\frac{\sigma_{\text{MCSE}}}{\text{median}[p(\Sigma y)]}$ Right: $\widehat{R}$ associated with the fit parameter $\Sigma$ . Both are shown for all $11 \cdot 12$ binned fits to the asymmetry $A(\phi)$ . The critical values that should not be exceeded are marked by dashed lines. . . . .	61
4.13	Left: relative error $\frac{\sigma_{\text{MCSE}}}{\text{median}[p(\Sigma y)]}$ Right: $\widehat{R}$ associated with the fit parameter $\Sigma$ . Both are shown for all $11 \cdot 12$ unbinned fits. The critical values that should not be exceeded are marked by dashed lines. . . . .	62
4.14	Posterior predictive check using the draws of the detector coefficients $a$ and $b$ for the kinematic bin $1250 \text{ MeV} \leq E_\gamma < 1310 \text{ MeV}, 0 \leq \cos \theta < 0.17$ . Points with error bars are the polarization weighted sum of event yields. The dashed line is the mean of the predictive values while the solid opaque lines are representative of one simulation draw $a^{(s)}, b^{(s)}$ . . . . .	63
4.15	Final results for the beam asymmetry $\Sigma$ in $\eta$ photoproduction off the proton for all kinematic bins obtained with BAYESIAN methods. They are compared with the results of a least squares fit and an unbinned fit as given in reference [Afz19]. All results agree within statistical error bars or within the widths of marginal posterior distributions.	65
4.16	Normalized residuals (left) and unaltered distribution (right) of all 10000 fits for the beam asymmetry $\Sigma = (1 - \delta) \cdot \Sigma_1 + \delta \cdot \Sigma_2$ . GAUSSIAN fits are performed with results given on top of each plot. . . . .	67
4.17	Normalized residuals (left) and unaltered distribution (right) of all 10000 fits for the background beam asymmetry $\Sigma_t^{\text{bkg}}$ . GAUSSIAN fits are performed with results given on top of each plot. . . . .	68
4.18	Fitted efficiency function (red line) applied to the polarization weighted sum of event yields (data points) for one toy Monte Carlo bin. 12 bins in $\phi$ are built for demonstration. . . . .	68
4.19	Combined (added) posteriors of all 1000 fits. Left: Signal beam asymmetry $\Sigma_1$ Right: Background beam asymmetry $\Sigma_t^{\text{bkg}}$ . A GAUSSIAN fit is performed with results given on top. . . . .	69
4.20	Combined (added) posteriors of all fits for the fit parameter $\Sigma_2^{\text{true}}$ . A GAUSSIAN fit is performed which reproduces exactly the values that were used for the simulations. . . . .	70

4.21 MCMC diagnostics for the event based BAYESIAN fit. Left: MCSE, Right: $\widehat{R}$ -value. The critical values not to be exceeded are marked by the dashed lines. . . . .	71
4.22 Posterior predictive checks of one toy Monte Carlo bin using the draws from the marginal posteriors of the detector coefficients $a, b$ (opaque blue lines). The mean values are marked by the dashed line and follow the distribution of the data points which are the polarization weighted sum of event yields, using 12 $\phi$ bins. . . . .	71
4.23 Final results for the beam asymmetry $\Sigma$ in $\eta'$ photoproduction. Two sets of results are shown: The dark blue distributions and orange data points with errorbars are obtained with an unbinned fit that does not consider any background contributions. The light blue distributions and data points are obtained with the modified BAYESIAN fit and by correcting the point estimates according to Equation (4.42), respectively. All errors are statistical errors only. . . . .	73
4.24 Results for the additionally fitted $\Sigma_2^{\text{true}}$ (distributions) compared with the underlying data points [Mah22] with statistical errors. The error bars on average cover $1\sigma$ of the distributions, indicating a successful fit. All errors are statistical errors only. . . . .	74
4.25 MCMC diagnostics for the event based BAYESIAN fit. Left: MCSE, Right: $\widehat{R}$ -value. The critical values not to be exceeded are marked by the dashed lines. . . . .	75
4.26 Posterior predictive checks of the kinematic bin $1700 \text{ MeV} \leq E_\gamma < 1800 \text{ MeV}, 0.67 \leq \cos \theta < 1$ using the draws from the marginal posteriors of the detector coefficients $a, b$ (opaque blue lines). The mean values are marked by the dashed line and follow the distribution of the data points which are the polarization weighted sum of event yields, using 12 $\phi$ bins. . . . .	75
4.27 Final results for the beam asymmetry $\Sigma_{\eta'}$ for all energy and angular bins. Only the corrected results from the unbinned maximum likelihood fit and distributions from the modified BAYESIAN fit are shown. The bottom of each plot indicates the systematic error as gray bars. It was determined as previously discussed. . . . .	77
5.1 Results for the beam asymmetry $\Sigma_{\eta'}$ (orange errorbars and distributions) compared with the results for the energy bins $E_\gamma = 1569 \text{ MeV}, E_\gamma = 1676 \text{ MeV}, E_\gamma = 1729 \text{ MeV}$ reported in reference [Col+17] (black errorbars). Systematical errors are shown as grey bars. . . . .	80
5.2 Results for the beam asymmetry $\Sigma_{\eta'}$ (orange errorbars and distributions) compared with PWA solutions: etaMAID [Tia+18](dashed black line), . . . The errorbars only depict statistical error, the systematic error is shown as grey bars. . . . .	82
A.1 Coplanarity $\Delta\phi$ for all energy and angular bins. Data points are displayed as open circles, scaled Monte Carlo data belonging to $\eta'$ photoproduction is displayed as solid histogram. The determined cut ranges are indicated by the dashed red lines. . . . .	89
A.1 Coplanarity $\Delta\phi$ for all energy and angular bins. Data points are displayed as open circles, scaled Monte Carlo data belonging to $\eta'$ photoproduction is displayed as solid histogram. The determined cut ranges are indicated by the dashed red lines. . . . .	90
A.2 Polar angle difference $\Delta\theta$ for all energy and angular bins. Data points are displayed as open circles, scaled Monte Carlo data belonging to $\eta'$ photoproduction is displayed as solid histogram. The determined cut ranges are indicated by the dashed red lines. . . . .	91

---

A.2	Polar angle difference $\Delta\theta$ for all energy and angular bins. Data points are displayed as open circles, scaled Monte Carlo data belonging to $\eta'$ photoproduction is displayed as solid histogram. The determined cut ranges are indicated by the dashed red lines. . . . .	92
A.3	Missing mass $m_x$ for all energy and angular bins. Data points are displayed as open circles, scaled Monte Carlo data belonging to $\eta'$ (black), $2\pi^0$ (yellow) and $\pi^0\eta$ (magenta) photoproduction is displayed as solid histogram while their sum is displayed as turquoise histogram. The determined cut ranges are indicated by the dashed red lines. . . . .	93
A.3	Missing mass $m_X$ for all energy and angular bins. Data points are displayed as open circles, scaled Monte Carlo data belonging to $\eta'$ (black), $2\pi^0$ (yellow) and $\pi^0\eta$ (magenta) photoproduction is displayed as solid histogram while their sum is displayed as turquoise histogram. The determined cut ranges are indicated by the dashed red lines. . . . .	94
A.4	Invariant mass $m_{\text{meson}}$ for all energy and angular bins. Data points are displayed as open circles, scaled Monte Carlo data belonging to $\eta'$ (black), $2\pi^0$ (yellow), $\pi^0\eta$ (magenta), $\pi^0$ (green) and $\omega$ (blue) photoproduction is displayed as solid histogram while their sum is displayed as turquoise histogram. The determined cut ranges are indicated by the dashed red lines. . . . .	95
A.4	Invariant mass $m_{\text{meson}}$ for all energy and angular bins. Data points are displayed as open circles, scaled Monte Carlo data belonging to $\eta'$ (black), $2\pi^0$ (yellow), $\pi^0\eta$ (magenta), $\pi^0$ (green) and $\omega$ (blue) photoproduction is displayed as solid histogram while their sum is displayed as turquoise histogram. The determined cut ranges are indicated by the dashed red lines. . . . .	96
B.1	Fit performance in dependence of the number of bins. Left axis shows the mean $\mu$ of the distribution of the normalized residuals $\xi$ , right axis shows the mean $\chi^2$ of all fits. Squares simulate fits with statistics similar to the $\gamma p \rightarrow p\eta' \rightarrow p\gamma\gamma$ final state, triangles statistics similar to the $\gamma p \rightarrow p\eta \rightarrow p\gamma\gamma$ and final state, pentagons statistics similar to the $\gamma p \rightarrow p\pi^0 \rightarrow p\gamma\gamma$ . Dotted red line indicates the ideal value of $\chi^2 = 1$ , while the dashed blue line indicates the ideal mean of the normalized residuals at $\mu = 0$ . . . . .	98
C.1	Combined posteriors of all 1000 fits without truncation for the signal beam asymmetry $\Sigma_1$ and the background beam asymmetry $\Sigma_t$ . Left: normalized residuals $\Xi$ , Right: unaltered added posterior distributions. GAUSSIAN fits have been performed with results given on top of each plot. . . . .	100
C.2	Posterior distributions of $\Sigma_1$ (left) and $\Sigma_t$ (right) combined in an independent likelihood pool. GAUSSIAN fits to the distribution confirm the reproduction of the input values within $1\sigma$ . Note that only very few datapoints were available for the fits, because the distributions overwhelmingly converge into a single bin at $\pm 0.5$ , hence the large errors on the fit parameters. . . . .	101

# List of Tables

---

1.1	Summary of the particles of the SM . . . . .	1
1.2	Allowed quantum numbers for the intermediate resonance state $N^*/\Delta^*$ . . . . .	4
3.1	The five most probable decay modes of the $\eta$ and $\eta'$ meson. The most probable further decay with according branching ratio is shown in brackets.[Wor+22] . . . . .	17
3.2	Examined MC reactions that were used in sum for the fit . . . . .	23
3.3	Fit functions and cut ranges for each kinematic variable . . . . .	24
3.4	Total cross sections $\sigma$ in the energy range 1500 to 1800 MeV, branching ratios (BR) to $n\gamma$ final states, maximum acceptance $\tilde{A}$ for signal and possible background contributions as well as the expected signal to background ratio $R$ . References [Die+20] and [Käs+18] give the cross sections only up to roughly 1500 MeV, the given values are thus upper bounds. For the same reason, from reference [Sta+11] only a lower bound can be estimated. For all other reactions a rough mean over the energy bins of interest is built. If the references provide only differential cross sections a crude integration in each angular bin is performed. In case only very few ( $O(10^1)$ ) decays pass event selection, the acceptance is built in one global bin only for the respective reactions. This is indicated by the horizontal line. . . . .	32
3.5	Relative loss in signal and background events if a cut on $\Delta E$ is applied. . . . .	38
4.1	Summary of the complete setting of all toy Monte Carlo experiments for the event based fit. Values and table layout adapted from [Afz19]. . . . .	55
4.2	Summary of the complete setting of all toy Monte Carlo experiments for the event based fit. Table layout adapted from [Afz19]. . . . .	66